Journal of Materials Chemistry A

ROYAL SOCIETY OF CHEMISTRY

PAPER

View Article Online
View Journal

Cite this: DOI: 10.1039/d6ta01058j

Effect of electrochemical etching parameters on the morphology and photocatalytic activity of porous 4H-SiC flakes

Vanessa Spanò, †[a] Matteo Barcellona, †[c] Angelo Ferlazzo, [a] Marcello Condorelli,[a] Luca Calantropo, [a] Roberto Fiorenza,[a] Salvatore Scirè, [a] Antonino Gulino, [b] Thomas Defforge,[c] Gaël Gautier[c] and Maria Elena Fragalà *[b]

Porous silicon carbide (SiC), with peculiar chemical modifications, can act as a catalyst that enhances stability, selectivity, and sustainability, offering distinct advantages over conventional oxides and carbon substrates as well as bulk SiC. In particular, the 4H-SiC polytype represents a versatile material platform that connects electronic, photonic, mechanical, and quantum functionalities with exceptional robustness, high thermal conductivity, and chemical inertness. While wet etching methods are largely ineffective due to SiC's chemical resistance, electrochemical etching (ECE) provides a powerful route to fabricate thin membranes and porous structures by exploiting dopant-defined regions. Under anodization in hydrofluoric acid-based electrolytes, crystalline material etching yields diverse pore morphologies—spongy, triangular, chevron, dendritic, sinuous, or columnar—strongly influenced by doping, current density, or carrier photogeneration. In this work, we present an extended study on optimizing ECE conditions to tailor the properties of porous 4H-SiC flakes resulting from the etching of SiC wafers under specific operational conditions. Notably, the different etch mechanisms governing the silicon- and carbon-terminated faces produce distinct porosity profiles and, even more relevant, affect the electronic properties and therefore the photocatalytic activity of the obtained SiC flakes. Accordingly, photocatalytic performances are evaluated by following the degradation of organic dyes in water and bio-reforming processes for hydrogen evolution, validating porous SiC flakes as a promising material for environmental remediation and renewable energy production.

Received 3rd February 2026
Accepted 9th April 2026

DOI: 10.1039/d6ta01058j

rsc.li/materials-a

Introduction

The global energy landscape is undergoing profound transformations, driven by the urgent need to mitigate climate change, reduce dependence on fossil fuels, and secure sustainable pathways for industrial development. Hydrogen has long been recognized as a cornerstone of this transition, offering a clean, high-energy fuel that produces only water upon combustion.[1]

Yet, despite its promise, hydrogen production remains dominated by fossil-based processes such as steam methane reforming, which undermines its potential as a truly "green" energy carrier. To overcome this limitation, photocatalysis has emerged as a radically different approach: in particular, semiconductor-based photocatalysis has emerged as one of the most promising strategies for converting abundant solar energy into chemical fuels while simultaneously addressing environmental pollution.[2,3]

By harnessing sunlight to drive chemical reactions, semiconductor materials can split water and/or reform organic substrates into hydrogen without the carbon footprint of conventional technologies. This dual functionality—simultaneous energy generation and pollutant remediation—positions photocatalysis as a key enabler of next-generation sustainable systems.[4] For example, photoreforming of organic wastewaters is an advantageous alternative to water splitting since it overcomes the thermodynamic and kinetic constraints of oxygen evolution reaction (OER) and valorizes the wastewater streams, thus representing a synergistic strategy toward both clean energy generation and environmental remediation.[5] Another interesting approach is the photoelectrochemical conversion (PEC) of CO_2.[6]

Since the pioneering work of Fujishima and Honda on TiO_2 photoanodes,[7] titanium dioxide has dominated the field due to its stability, non-toxicity, and wide bandgap.[8] However, TiO_2 suffers from intrinsic limitations: its activity is restricted to

[a]Department of Chemical Sciences, University of Catania, Viale Andrea Doria, 6, 95125-Catania, Italy

[b]Department of Chemical Sciences, University of Catania and INSTM UdR Catania, Viale Andrea Doria, 6, 95125-Catania, Italy. E-mail: me.fragala@unict.it

[c]GREMAN UMR-CNRS 7347, INSA Centre Val de Loire, Université de Tours, Tours, France

† Authors equally contributed.

ultraviolet light, which represents only a small fraction of the solar spectrum,[4] and its designation as a critical raw material in several countries has raised concerns about long-term availability.[9] These challenges have spurred intense research into alternative photocatalysts that combine efficiency, robustness, and abundance.

N-type semiconductors, such as ZnO, $BiVO_4$, WO_3, perovskite, and many other photoactive materials, are exploited as photoanodes to promote the reduction of CO_2.[10,11]

Semiconductor nanomaterials, including metal oxides, sulfides, nitrides, and emerging hybrid structures, enable efficient solar-driven degradation of organic pollutants and hydrogen evolution, owing to their tunable band structures, high surface reactivity, and capacity to generate charge carriers under illumination.[12–15]

Among the semiconductors used as photocatalysts, silicon carbide (SiC) has emerged as particularly promising due to its chemical inertia and mechanical and thermal stability, making it suitable to work in harsh conditions.

SiC is a wide bandgap semiconductor distinguished by exceptional mechanical strength, high electron saturation velocity, and remarkable chemical inertness.[16,17] Its polytypism—over ~200 reported structures—offers unique opportunities to tailor physical and structural properties.[18] Of these, the 4H polytype has become predominant in microelectronics and high-power applications, owing to its bandgap of 3.2 eV, high breakdown field, and radiation resistance.[19] Beyond electronics, 4H-SiC exhibits properties highly relevant to photocatalysis: polar surfaces with distinct chemistries, high thermal conductivity, and oxidation resistance. These attributes make it an attractive candidate for environmental and energy applications, particularly when engineered into porous structures that maximize surface area and facilitate charge transfer.[20]

Fabrication of porous SiC, however, presents challenges. Conventional wet etching methods are largely ineffective due to SiC's chemical resistance, while dry etching techniques such as reactive ion etching (RIE) can damage substrates and require costly equipment.[16] The electrochemical etching (ECE) offers a compelling alternative.[21] By exploiting dopant-defined regions and carefully controlled current densities, ECE can produce diverse porous morphologies—spongy, dendritic, columnar, or chevron—depending on crystallographic orientation and etching conditions. Importantly, etching on the carbon-terminated face proceeds at roughly twice the rate of the silicon-terminated face, yielding distinct porosity profiles. While porous SiC has been explored for biosensors,[22] photocathodes, and implantable devices,[23] its potential as a photocatalyst remains underexplored.

Recent studies have demonstrated that porous 4H-SiC flakes, often considered industrial by-products of ECE, can be repurposed for photocatalytic applications.[10] Their high surface area enhances pollutant adsorption, while their tunable bandgap enables efficient charge separation under illumination. Moreover, the valorization of these flakes aligns with principles of the circular economy, transforming waste into functional materials for environmental remediation and renewable energy production.[20] In particular, porous 4H-SiC has shown promise in degrading organic dyes and driving hydrogen evolution through glycerol photoreforming—a process that not only generates clean fuel but also adds value to biomass by utilizing glycerol, a by-product of biodiesel production.[24,25]

Despite these advances, critical questions remain regarding the optimization of etching conditions to control morphology, bandgap, and photocatalytic performance. The relationship between current density, crystallographic orientation, and pore structure is complex, and systematic studies are needed to establish design rules for tailoring porous SiC toward specific applications. Furthermore, while TiO_2 has set the benchmark for photocatalysis, the potential of SiC to serve as a sustainable alternative—combining robustness, recyclability, and multifunctionality—has yet to be fully validated.

In this work, we present an extended study on the optimization of ECE conditions for 4H-SiC, focusing on the regulation of porous flake morphology and bandgap values. We demonstrate how these parameters influence photocatalytic performance in two representative applications: degradation of organic dyes and hydrogen evolution *via* glycerol photoreforming. By repurposing industrial byproducts and leveraging the unique properties of SiC, this study advances the case for porous 4H-SiC as a next-generation photocatalyst, bridging environmental remediation and renewable energy production.

Materials and methods

Methodology

This work investigates the properties of porous SiC flakes derived from the electrochemical etching process of SiC wafers in terms of absorption, advanced oxidation processes (AOP), and hydrogen production. Specifically, the material's porosity and semiconductor properties suggest its potential for environmental remediation, particularly in water purification and hydrogen production. Studies will therefore be considered regarding (i) the absorption of anionic and cationic dyes with different structures and their photodegradation capacity, with a view to their applicability as photoactive absorbers, and (ii) hydrogen production from glycerol photoreforming processes.

Dye concentration was monitored in mol L^{-1}, and the photocatalytic degradation efficiency was expressed as removal percentage (%). Hydrogen production was quantified in μmol and normalized to catalyst mass and irradiation time, expressed as μmol g^{-1} h^{-1}.

The material's characterization will focus on the morphology of the porous flakes as a function of ECE conditions and their impact on surface area (m^2 g^{-1}) and pore size (nm), as well as the determination of the band gap (eV), determined using complementary methodologies also useful for determining the Fermi level (eV), the position of the HOMO and LUMO levels (eV), and the surface composition (at%).

Preparation of porous 4H-SiC flakes *via* ECE

In this work, 4-inch 4H-SiC n-type wafers (MSE Supplies 4° off-axis with resistivity of 0.015–0.028 Ω cm, thickness of 350 ± 25 μm, roughness <5 nm on C-face and <1 nm on Si-face) have

been used in the ECE process for the preparation of the porous 4H-SiC flakes. The periphery of the 4H-SiC wafers have been previously coated with a thin layer of Ti (about 20 nm) and Ni (about 100 nm) bilayer through the evaporation technique (MBE550S, Plassys) and annealed at a temperature of 1100 °C for 180 s to obtain the Ti/Ni alloy. The deposition is necessary to establish an ohmic contact between the SiC and the gold tips that are placed around the etched surface.

The ECE process is performed inside a specific electrochemical cell of 6 inches in PS designed by the GREMAN laboratory and fabricated by AMMT GmbH®. The cell indeed possesses a specific collector that serves to accumulate the porous flakes created during or after the etching process. The circular area of the etched wafer is about 23.7 cm^2 (with a diameter of the O-ring of 5.5 cm). The employed electrolyte solution is composed of hydrofluoric acid (HF, with a concentration of 5 wt%, 15 wt%, or 30 wt%), acetic acid (AA, with a concentration of 10 wt%), in deionized water.[26] The ECE processes were carried out in galvanostatic mode by applying "on–off" pulsed current (applying current densities at 42 or 420 mA cm^{-2}) with a duration of 2 s while no current is applied during 5 s of offset and using the PSI8000 source, at room temperature and pressure, for etching times varying from 1 hour and 30 minutes to 4 hours. After ECE, the samples were rinsed in deionized water in the Quick Dump System (QDR) for 5 cycles.

SiC ECE is a two-step reaction. The first reaction is a two-path electrochemical oxidation that is described by eqn (1) and (2) below:

$$SiC + 2H_2O + 4h^+ \rightarrow SiO_2 + CO + 4H^+ \quad (1)$$

$$SiC + 4H_2O + 8h^+ \rightarrow SiO_2 + CO_2 + 8H^+ \quad (2)$$

Water is required to form silicon oxide on the surface of the silicon carbide, which occurs when about eight holes reach the interface.[21,27]

In the second reaction, the dissolution of the oxide is driven by the HF present in the electrolyte solution (eqn (3)):

$$SiO_2 + 6HF \rightarrow 2H^+ + SiF_6^{2-} + 2H_2O \quad (3)$$

It is generally admitted that the ECE of SiC mechanism is governed by holes as charge carriers.[28]

When considering the anodic oxidation of silicon carbide, one of the most striking features is the pronounced anisotropy between the C-face $(000\bar{1})$ and the Si-face (0001). The C-face, terminated by carbon atoms, requires simultaneous removal of carbon species—typically as CO or CO_2—during oxidation. The kinetics of this process are faster than the Si-face,[21] and the resulting oxide has an inferior quality, tends to be less uniform, often incorporating defects or roughness that affect its electrical properties.

In contrast, the Si-face, which terminates in silicon atoms, exhibits a lower and more controlled oxidation rate, leading to the formation of a smooth and stable SiO_2 film.

The ECE experiment employed in this study has been summarized in the following table (Table 1):

The effects of current density and HF concentration in the ECE process of 4H-SiC were analyzed through a one-factor-at-a-time (OFAT) approach, considering Batch I as a reference, and one variable was changed at a time. In Batch I, previously investigated,[20] the flakes exhibit medium porosity with a heterogeneous distribution (*vide infra*).

In Batch II, the HF concentration was kept constant at 15 wt%, reducing the applied current density by a factor of 10, from 420 to 42 mA cm^{-2}, to analyze how current density influences the pore morphology on the flakes.

In Batches III and IV, the same current density of 420 mA cm^{-2} of Batch I was used to prepare the porous flakes, but the HF concentration was reduced by 3 times (5 wt%) or increased by 2 times (30 wt%), respectively, to understand the influence of electrolyte composition on the porous morphology of the flakes.

Investigation methods

Field emission scanning electron microscope (FE-SEM) measurements

FE-SEM images were acquired with a Jeol JSM-7900F at 10 kV using the in-lens (UED) detector, a 4 mm working distance, and a chamber pressure of 3×10^{-3} Pa. The porous 4H-SiC flakes of both faces were randomly deposited on carbon tape to allow imaging in top- and cross-section views.

UV-Vis measurements for dye adsorption and photocatalytic degradation

The adsorption and photocatalytic experiments were carried out by monitoring the decrease in dye concentration in 5 mL aqueous solutions, with 2 mg of porous flakes. The initial dye concentration was 1.5×10^{-5} M for Methylene Blue (MB), Rhodamine 6G (Rh6G), and Rhodamine B (RhB), and 3.0×10^{-5} for Methyl Orange (MO), using UV-Vis spectroscopy (Jasco V-530).

In order to ensure adsorption–desorption equilibrium, the dye solutions with the porous flakes were kept in the dark for 24 h, followed by irradiation under a 365 nm UV-lamp for 4 h in static conditions. Initially, the MB was employed as a representative model dye to evaluate both the adsorption capacity of the 4H-SiC flakes and the photocatalytic activity of all the porous samples. Other dyes as RhB, Rh6G, and MO were then investigated for photocatalytic degradation.

X-ray photoelectron spectroscopy (XPS)

XPS spectra were measured at 45° take-off angle relative to the surface normal with a PHI 5000 Versa Probe II system (ULVAC-

Table 1 ECE parameters used in the production of porous 4H-SiC flakes

Experimental batches	HF [wt%]	Current density (mA cm^{-2})
Batch I (previous work)[20]	15	420
Batch II	15	42
Batch III	5	420
Batch IV	30	420

PHI, INC. base pressure of the main chamber 1×10^{-8} Pa).[29,30] Samples were excited with a monochromatized Al Kα X-ray radiation using a pass energy of 5.85 eV. Spectra calibration was achieved by fixing the Ag $3d_{5/2}$ peak of a clean sample at 368.3 eV.[31] The instrumental energy resolution was 0.5 eV. The XPS valence band spectra were obtained by accumulating 50 cycles in a $-1 \rightarrow 20$ eV energy range, using a 2.95 pass energy and 0.025 eV per step. The XPS peak intensities were obtained after a Shirley background removal.[29] The atomic concentration analysis was performed by considering the relevant atomic sensitivity factors.[29,30]

Brunauer–Emmett–Teller (BET) and Barrett–Joyner–Halenda (BJH) methods

The textural properties of the samples were analyzed by N_2 adsorption–desorption at −196 °C by using Micromeritics ASAP 2020 instrument. Surface area and the pore size distribution were determined by Brunauer–Emmett–Teller (BET) and Barrett–Joyner–Halenda (BJH) methods, respectively. Samples were previously outgassed at 100 °C overnight.

UV-Vis spectroscopy for optical bandgap evaluation

Optical bandgaps estimations were obtained through UV-Vis diffuse reflectance using a Cary 60 UV-Vis spectrophotometer equipped with the "Barellino" tool by Agilent Technologies. Spectra were collected over the 200–800 nm range and recorded as Kubelka–Munk units *versus* wavelength. The optical band gaps of the obtained porous flakes were then estimated using Tauc plots.

Electrochemical measurements

Electrochemical analyses were conducted using a DropSens μStat 400 potentiostat (DropSens, Spain), powered by Dropview 8400 data acquisition software for cyclovoltammetry (CV) analyses. CV analyses were conducted in anhydrous acetonitrile in the presence of a supporting electrolyte (tetrabutylammonium benzoate, 0.1 M), in the −3 to 3 V potential range. Electrochemical measurements were performed using screen-printed carbon electrodes (SPCE) purchased from Metrohm-DropSens (Metrohm Italiana S.r.l., Origgio (VA), Italy). The SPCE consisted of a planar substrate with both auxiliary and working electrodes (4 mm diameter and 0.1257 cm^2 geometric area) of carbon, while the reference electrode was Ag/AgCl.[32]

Hydrogen evolution reaction (HER) measurements

HER tests were performed in a batch photocatalytic reactor containing 50 mg of SiC sample and 50 mL water/glycerol (20% v/v) solution. The suspension was irradiated for 5 h with an Osram Ultra Vitalux solar lamp (300 W, 10.7 mW cm^{-2}). Before irradiation, Ar was bubbled for 1 h. H_2 was quantified by GC-TCD (Agilent 6890, Supelco Carboxen 1000 column).[33] The H_2/CO_2 ratio of the glycerol photoreforming reaction was measured by the GC-TCD after the appropriate standard calibrations. All the tests were carried out in triplicate, and the reported error bars represent the standard deviation of three independent measurements (typical relative error = 3%).

Results and discussion

Characterization analyses of the porous 4H-SiC flakes

The influence of ECE parameters on the morphology of porous 4H-SiC flakes was examined by SEM.

Both Si-face and C-face flakes were analyzed in top-view and cross-section images to assess the effects of HF concentration and current density on surface and in-depth morphologies.

Top-view images of the Si-face flakes (Fig. 1) revealed that by decreasing current density while keeping constant HF concentration (Fig. 1b), larger pores are produced compared to Batch I (Fig. 1a), while variations in HF concentration (5–30 wt% – Fig. 1c and d) at constant current density (420 mA cm^{-2}) did not significantly alter the cauliflower-like features of surface morphology. This behavior is in good agreement with the controlled oxidation process during ECE, leading to a relatively uniform SiO_2 formation during the ECE process, which is removed at a similar etch rate by HF. Current density was considered the principal driving force of pore formation and morphology.

Cross-sectional analyses showed distinct depth morphologies (Fig. S1): Batch I shows a dendritic-like morphology (Fig. S1a), Batch II exhibited a stratified structure (Fig. S1b), Batch III an empty-columnar layered morphology with ∼100 nm pore length (Fig. S1c), and Batch IV a columnar-like structure (Fig. S1d) similar to Batch III.

From the cross-section analyses of Si-face flakes, the etching process affects in-depth pore growth more than the surface morphology, and variations in both HF concentration and current density lead to different depth morphologies.

In contrast, the C-face displayed greater sensitivity to the ECE parameters. Top-view SEM (Fig. 2) showed that, compared to the C-face flakes of Batch I (Fig. 2a), a spongy-like morphology with triangular and spherical macropores is observed for Batch II (Fig. 2b), a random rough surface with poorly defined pores is observed for Batch III (Fig. 2c), and nanoporous spongy structures with spherical features for Batch IV (Fig. 2d).

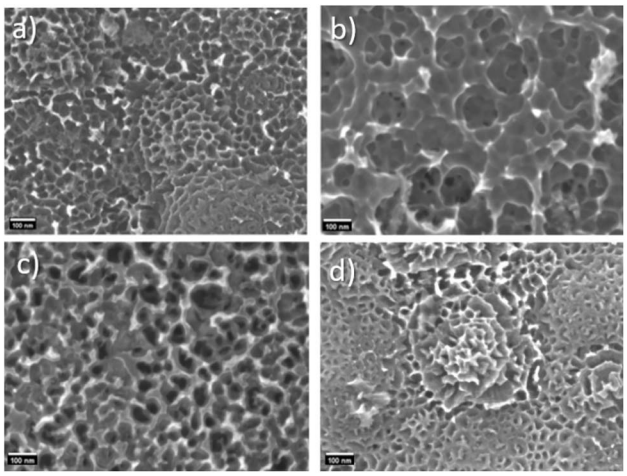

Fig. 1 Comparison of all 4H-SiC porous flakes for on-top-view SEM analyses of Si-face at the same magnification (150.000×): (a) Batch I; (b) Batch II; (c) Batch III; (d) Batch IV.

Cross-sectional analyses revealed that most C-face flakes retained a columnar-like structure along the [000$\bar{1}$] axis, independent of parameter variations (Fig. S2a–d). Only Batch III (Fig. S2c) exhibited a multilayer structure, similar to the Si-face under the same conditions (420 mA cm^{-2}, 5 wt% HF), thus suggesting that pulsed current combined with low HF concentration can induce comparable depth morphologies on both faces.

In general, for all the ECE experiments, the C-face flakes possess a comparable columnar-like structure directed along the [000$\bar{1}$] axis, independent of parameter variations. Overall, current density governs pore size and morphology on the Si-face, while HF concentration exerts limited influence under constant current density.

The C-face, however, exhibits distinct surface morphologies under varying ECE conditions, though its depth structure remains largely columnar. These findings highlight the anisotropic response of 4H-SiC to ECE and underscore the importance of crystallographic orientation in controlling porous structure formation. High current accelerates the ECE process more than HF concentration, thus causing defect formation, pit coalescence, and macropore emergence, lowering surface area and affecting uniformity. HF concentration, by contrast, tunes dissolution rates and wall thinning without disrupting pore ordering.

Brunauer–Emmett–Teller (BET) and Barrett–Joyner–Halenda (BJH) analyses have been performed to estimate the surface area, and the mean pore diameters of the Si-face and C-face flakes for all the Batches, and the resulting values are listed in Table 2 below. Compared with Batch I, both Si-face and C-face flakes of Batch II exhibit the lowest surface areas, accompanied by bimodal pore size distributions, with two maxima (Fig. S3). The major presence of macropores (pore diameter > 50 nm) in the C-face samples indicates that larger pores are preferentially formed with these materials. In contrast, the Si-face flakes of Batch III achieve the highest surface area (49.6 m^2 g^{-1}) and display a relatively narrow pore size distribution centered at 23.4 nm, characteristic of the prevalent presence of mesopores (pore diameter between 2 and 50 nm).

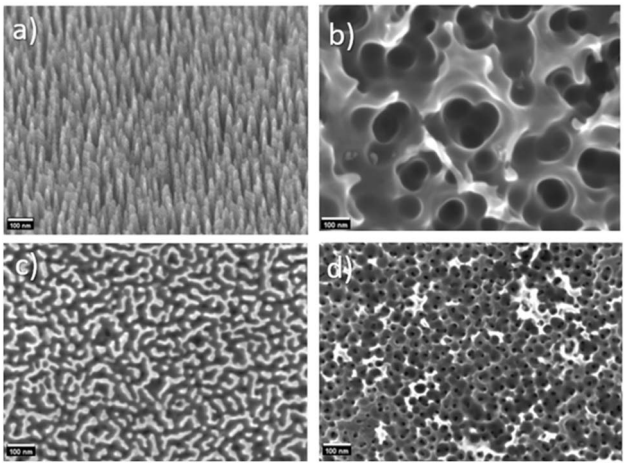

Fig. 2 Comparison of all 4H-SiC porous flakes on-top-view SEM images of C-face at the same magnification (150.000× – scale bar 100 nm): (a) Batch I; (b) Batch II; (c) Batch III; (d) Batch IV.

Table 2 Textural properties of porous 4H-SiC flakes, including surface area and mean pore distribution for porous SiC flakes obtained under different ECE conditions

Samples	Surface area (m^2 g^{-1})	Mean pore diameters (nm)
C-face (Batch I)	36.4	59.4
Si-face (Batch I)	46.5	4.4 & 48.1
C-face (Batch II)	24.3	5.4 & 59.0
Si-face (Batch II)	28.8	31.8
C-face (Batch III)	30.2	7.0 & 31.0
Si-face (Batch III)	49.6	23.4
C-face (Batch IV)	22.7	6.0 & 49.7
Si-face (Batch IV)	30.8	30.1

The corresponding C-face flakes of Batch III retain a bimodal distribution, suggesting less controlled pore formation (Fig. S4). The values obtained for Batch III are comparable to those of Batch I, highlighting the reproducibility of porosity when HF concentration is varied under constant current density. By comparison, Batch II, etched under altered current density but constant HF concentration, shows markedly reduced surface areas and broader pore distributions for both Si- and C-face flakes. Batch IV (Fig. S5) exhibits similar characteristics to Batch II, thus reinforcing the conclusion that current density exerts a stronger influence than HF concentration on the development of surface area and pore uniformity in porous SiC.

Photocatalytic behavior of the porous 4H-SiC flakes: dyes photodegradation in water

The photocatalytic removal of organic dyes from aqueous media represents a promising strategy within advanced oxidation processes (AOPs). In this study, porous 4H-SiC flakes prepared *via* ECE were evaluated for their ability to degrade Methylene Blue (MB) under UV irradiation. To decouple adsorption from photocatalytic oxidation, MB molecules were first equilibrated on the catalyst surface in the dark, followed by illumination with a 365 nm UV source. Adsorption experiments (Fig. 3) revealed significant Batch-dependent variations. Si-face flakes from Batch II exhibited enhanced MB uptake compared to Batch I,[20] while C-face flakes showed comparable adsorption behavior. The Si-face flakes of Batch III demonstrated the highest adsorption capacity, attributed to their increased surface area and modified pore size distribution. Despite this, both Batch II and III flakes displayed reduced photocatalytic efficiency relative to Batch I. Interestingly, Batch IV flakes combined high adsorption with improved photocatalytic activity compared to Batch II–III, thus suggesting a more favorable balance between surface morphology and electronic properties.

Photocatalytic degradation followed pseudo-first-order kinetics[34] listed in Table 3: the Si-face flakes of Batch I achieved the highest rate constant (2.52 × 10^{-3} min^{-1} M^{-1}), outperforming all other samples. The C-face flakes of Batch IV also exhibited relatively high activity (0.97 × 10^{-3} min^{-1} M^{-1}),

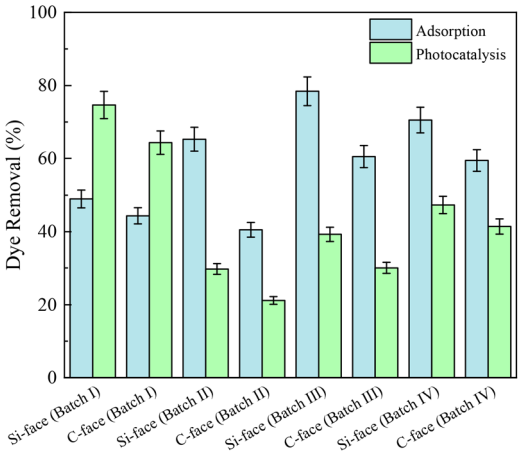

Fig. 3 Comparison of the photocatalytic behavior of porous 4H-SiC flakes of all the Batches with a 1.5×10^{-5} M solution of MB (pH = 7).

highlighting the influence of etching parameters on catalytic performance.

The adsorption experiments with MB reveal that surface area and pore accessibility strongly influence the dye uptake. The Si-face flakes from Batch III, characterized by their high surface area and uniform mesopores, exhibit the strongest adsorption performance.

Notably, even the Batch II Si-face flakes, despite possessing a lower surface area, show improved methylene blue uptake compared with Batch I, indicating that factors such as pore connectivity and surface chemistry (*e.g.*, hydroxylation) also contribute to adsorption.

However, strong adsorption does not necessarily translate into superior photocatalytic performance. The Batch I Si-face flakes achieve the highest pseudo-first-order rate constant (2.52×10^{-3} min^{-1} M^{-1}), outperforming all other samples despite their only moderate adsorption capacity. In contrast, Batches II and III, although effective adsorbers, display diminished photocatalytic activity. This divergence highlights the dominant role of electronic properties, defect density, charge recombination behavior, and surface states in governing photocatalysis once a baseline adsorption threshold is met. Batch I's enhanced performance likely arises from a favorable balance between structure and electronic quality. The moderate current density used during fabrication generates adequate surface area and accessible mesopores while limiting etch-induced defects that would otherwise serve as recombination centers.[35] The Si-face enables efficient electron–hole separation and charge transfer to the solution, sustaining radical formation under UV illumination. By comparison, Batches II and IV might be richer in defects that trap charge carriers and promote recombination, thereby limiting photocatalytic efficiency despite high adsorption.

Even so, the C-face, typically associated with bimodal pore structures and macropore formation (Table 2), can, as seen in Batch IV, deliver relatively high activity (0.97×10^{-3} min^{-1} M^{-1}) when current density is carefully controlled to reduce recombination pathways.

Both the Si-face and C-face flakes from Batch I exhibit the highest photocatalytic performance for methylene blue (MB) degradation. On this basis, these flakes were further evaluated using additional organic dyes—Rhodamine 6G (Rh6G), Rhodamine B (RhB), and Methyl Orange (MO)—to assess their broader photocatalytic response (Fig. 4).

Adsorption studies were performed at different pH values, according to the characteristics of dyes,[10] whilst photocatalytic experiments were conducted for 4 hours under illumination, without stirring, using a 365 nm UV lamp. The results were compared to those obtained for MB degradation at pH 7. Dye adsorption—and therefore subsequent photocatalytic degradation—depends not only on pore size, surface structure, and the electronic properties of the porous flakes, but also on the electrostatic interaction between the dye and the catalyst surface.

MO, being an anionic dye, exhibited neither adsorption nor degradation, thus confirming that electrostatic repulsion between MO and the negatively charged porous SiC surfaces inhibit photocatalytic activity, consistent with previous findings.[20] For cationic dyes such as Rh6G and RhB, earlier adsorption studies on porous SiC flakes[20] show that steric effects around the positively charged center govern adsorption efficiency. Since photocatalysis is a heterogeneous catalytic process, lower adsorption of the dyes results in reduced

Table 3 Photocatalytic degradation rate of all the porous 4H-SiC flakes for MB removal from water

Sample	Rate constant (min^{-1} M^{-1})
Si-face (Batch I)	$2.52 \times 10^{-3} \pm 0.13 \times 10^{-3}$
C-face (Batch I)	$1.86 \times 10^{-3} \pm 0.09 \times 10^{-3}$
Si-face (Batch II)	$0.62 \times 10^{-3} \pm 0.03 \times 10^{-3}$
C-face (Batch II)	$0.43 \times 10^{-3} \pm 0.02 \times 10^{-3}$
Si-face (Batch III)	$0.88 \times 10^{-3} \pm 0.04 \times 10^{-3}$
C-face (Batch III)	$0.64 \times 10^{-3} \pm 0.03 \times 10^{-3}$
Si-face (Batch IV)	$1.20 \times 10^{-3} \pm 0.06 \times 10^{-3}$
C-face (Batch IV)	$0.97 \times 10^{-3} \pm 0.11 \times 10^{-3}$

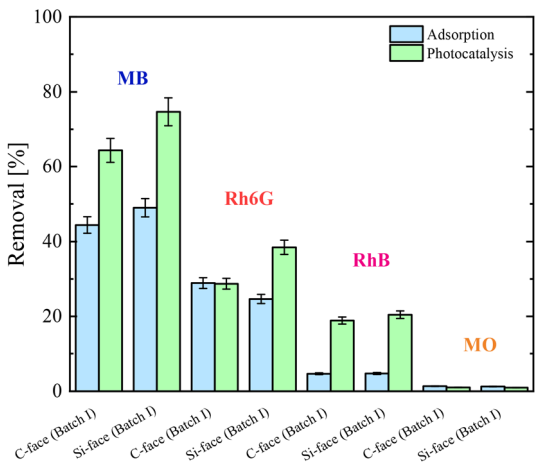

Fig. 4 Comparison of the absorption and photocatalytic behaviors of the porous 4H-SiC flakes with MB (pH 7), Rh6G (pH 5), RhB (pH 3), and MO (pH 7) with a concentration of 1.5×10^{-5} M.

photocatalytic activity compared to the MB photodegradation processes. In fact, from the graph in Fig. 4, the Si-face and C-face flakes exhibit the highest efficiency, both in adsorption and photocatalysis, in the presence of MB, followed by Rh6G and RhB, while no activity is observed with MO.

Optical band gap evaluation: Tauc plot

UV-Vis reflectance spectroscopy is used to evaluate the optical band gap of the flakes by the Tauc plot (Fig. S3).

Once the Kubelka–Munk function [$F(R)$] had been defined, the Tauc plot was constructed, *i.e.*, a graph correlating (eqn (4)):

$$[F(R_\infty)\cdot h\nu]^{1/n} = A(h\nu - E_g) \quad (4)$$

where $h\nu$ is the photon energy, n is a value that depends on the bandgap of the material (direct is $n = 1/2$, while indirect is $n = 2$), A is a constant, and E_g is the material bandgap value.

In this case, the 4H-SiC possesses an indirect bandgap, and the n value is $n = 2$ (eqn (5)):[36]

$$[F(R_\infty)\cdot h\nu]^{\frac{1}{2}} = A(h\nu - E_g) \quad (5)$$

The bandgap values of porous flakes obtained by varying the ECE conditions are reported in Table 4, and for all the batches, they were consistently lower than the bulk 4H-SiC wafer (3.2 eV). Fig. S6 shows the Tauc plot of the Si-face and C-face flakes from all the flakes batches, and the band gap energies were determined by extrapolating the linear part of the curves to $y = 0$.

The analysis revealed significant bandgap variations among the porous flakes. Bulk 4H-SiC wafers possess a bandgap of 3.2–3.3 eV,[37] whereas porous flakes exhibited reduced values due to ECE. Batch I Si-face flakes retained the highest bandgap (2.98 eV), closer to that of the bulk material, while all the other Batches show reduced bandgap values (ranging from 2.37 to 2.00 eV). The C-face flakes of Batch I also maintained relatively high bandgap values (2.69 eV). These shifts are attributed to oxide formation, amorphous regions, and defect states introduced during ECE,[38] which generate mid-gap levels and alter optical absorption. In fact, the observed color change of the flakes (from green-transparent wafer to goldish porous flakes) corroborates bandgap narrowing. The higher bandgap values of Batch I samples align with their superior photocatalytic activity, as excitation under 365 nm UV is more effective when the bandgap remains close to the bulk value. The results demonstrate that photocatalytic efficiency in porous 4H-SiC flakes is governed by a delicate interplay between morphological and electronic properties: increased surface area and porosity enhance dye adsorption, but excessive etching introduces defect states that lower the bandgap and promote charge carrier recombination. Consequently, samples with high adsorption capacity (Batch III and IV) exhibited reduced photocatalytic activity.

However, the definition of bandgap by the Tauc plot is affected by the quality of spectra and by the shape of the Urbach tail. Different slopes can be identified, and, accordingly, the band gap value cannot be easily estimated.[39] Accordingly, different approaches to check electronic band gap values have been proposed by using some test examples.

Table 4 Optical bandgap values of the porous 4H-SiC flakes of all the prepared batches obtained *via* the Tauc-plot

Sample	E_g^{opt} (eV)
Si-face (Batch I)	2.98
C-face (Batch I)	2.69
Si-face (Batch II)	2.37
C-face (Batch II)	2.22
Si-face (Batch III)	2.12
C-face (Batch III)	2.36
Si-face (Batch IV)	2.00
C-face (Batch IV)	2.35

Electrochemical determination of the porous 4H-SiC flakes bandgaps

Cyclic voltammetry was used to evaluate the electronic structure of the C-face flakes of Batches I, II, and IV, with particular attention to the resulting electrochemical bandgaps (Fig. 5). The working electrode was modified with 40 μL of a suspension of C-face flakes of Batches I, II, and IV with a mother solution of concentration 1 mg mL^{-1} in water.

The modified electrodes were left to dry at room temperature for 24 hours.[40]

The energy levels are reported with reference to the vacuum using the ferrocene/ferrocenium couple (Fc/Fc^+ = 4.80 eV *vs.* vacuum).[41] The values of oxidation and reduction offsets, HOMO, LUMO, and the electrochemical bandgap are listed in Table 5.

Data in Table 5 highlight that the C-face flakes of Batch II have the widest bandgap of the series, followed by the C-face of the I and IV Batches. From the CV analysis, it is possible to confirm the presence of mid-gap levels observed in the optical bandgap determination, which lead to an underestimation of the bandgap, especially for the C-face of Batch II, while the bandgaps of the C-face of the I and IV are similar to those determined with the Tauc plot.

In order to evaluate the redox of the C-face flakes from different Batches, it is necessary to determine the positions of the conduction band minimum (CBM) and valence band maximum (VBM) in terms of their potential (V *vs.* NHE). Considering that the CV experiments were carried out in anhydrous acetonitrile with reference to the vacuum using the ferrocene/ferrocenium, 0.630 V is the conversion constant[32] to apply to the oxidation and reduction onset (V *vs.* Ag/AgCl).[42] It is also necessary to consider that the ΔV of the Ag/AgCl *vs.* ferrocene/ferrocenium is 0.400 V. Hence, the final equation is (eqn (6)):

$$\begin{aligned} E_{V\ vs.\ NHE} &= E_{Fc/Fc^+} + 0.630\ V \\ &= \left(E_{Ag/AgCl} - 0.400\ V\right) + 0.630\ V \\ &= E_{Ag/AgCl} + 0.230\ V \end{aligned} \quad (6)$$

Table 6 below shows the oxidation and reduction onset potentials expressed in V *vs.* NHE calculated by applying the eqn (6):

The conduction band minimum (CBM) and valence band maximum (VBM) potentials of the C-face samples are plotted on the NHE scales in Fig. 6.

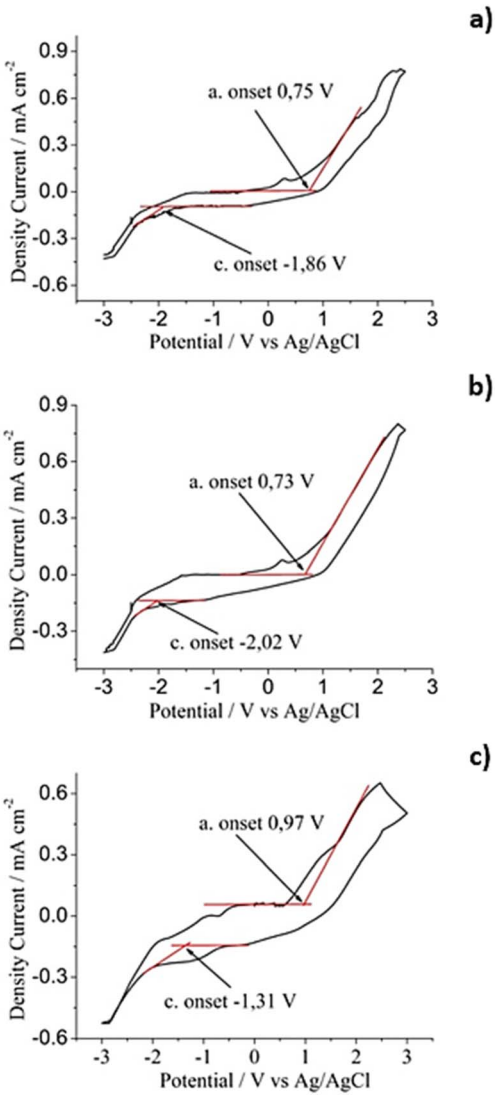

Fig. 5 Cyclic voltammogram *versus* the Ag/AgCl reference electrode of the C-face flakes of Batches I (a), II (b), and IV (c). The ΔV of the normal hydrogen electrode (NHE) *vs.* vacuum = 4.80 V; the ΔV of the Ag/AgCl *vs.* ferrocene/ferrocenium = 0.40 V; the ΔV of the ferrocene/ferrocenium *vs.* vacuum = 4.80 V.

C-face flakes of Batch II exhibit the most negative CBM with −1.79 V *vs.* NHE value, while C-face flakes of Batch IV show the most positive VBM with +1.20 V *vs.* NHE value, indicating the strongest reducing and oxidizing abilities of the series, respectively. The ability of the flakes to degrade MB closely follows their valence band position, controlling the oxidation pathways. In particular, the C-face from Batch II with the lowest VBM (+0.96 V *vs.* NHE) is the least active. C-face of the Batch I, even though its VBM is only slightly more positive (+0.98 V), is the best performing sample. Finally, C-face of Batch IV, despite having the highest VBM (+1.20 V), its activity remains moderate, attributed to the more aggressive ECE treatment, which increases amorphous content and defect sites, affecting charge separation and photocatalysis.

X-ray photoelectron spectroscopy (XPS) and electronic band gap evaluation

Fig. 7 shows the XPS valence band (VB) spectra for the three samples obtained by etching under different experimental conditions on a 4H-SiC wafer.

The observed valence band features are mostly Si 3p and C 2p in character, whose density of states extends several eV below (at higher binding energies) the valence band maximum (VBM), with the VBM itself being a crucial feature (often at the Γ point) for determining band offsets and electronic properties. In particular, the Si 3p states significantly contribute to the upper/outer parts of the valence band, while the C 2p orbitals mix with Si 3p states to form the core of the valence band structure. Therefore, the VBM energy position, relative to the Fermi level, is a major focus for heterojunction studies. VBM was determined by extrapolating a tangent to each spectrum at the point where the intensity falls rapidly near the Fermi level, and the obtained values are 1.95, 2.38, and 2.16 eV for the C-face of Batches IV, II, and I, respectively (Fig. 8).[43]

Literature studies report that the valence band maximum (VBM) for 4H-SiC (10 μm thick) was previously found at 1.8 eV, while that for the SiO_2/SiC system was measured at 2.2 eV.[43] Tab. S1 reports the surface atomic composition (at%) and related C/Si and O/Si ratio for the present samples: in particular, XPS O/Si ratios are 0.47, 0.33, and 0.35 for the C-face of Batch IV, II, and I, respectively. Therefore, all of them are consistent with the SiO_2/SiC stoichiometry. It emerges that the C-face of Batch IV contains the large SiO_2 surface concentration (24% SiO_2–76% SiC) while the stoichiometry of the C-face of Batch II is 16%

Table 6 Oxidation and reduction onset potentials in V *vs.* NHE of the C-face flakes of Batches I, II and IV

Sample	Ox (V *vs.* NHE)	Red (V *vs.* NHE)
C-face (Batch I)	+0.98	−1.63
C-face (Batch II)	+ 0.96	−1.79
C-face (Batch IV)	+ 1.20	−1.08

Table 5 CV measurements to determine the oxidation and reduction offsets, HOMO, LUMO, and electrochemical bandgap of the C-face flakes of the I, II, and IV Batches

Sample	Ox (V *vs.* Ag/AgCl)	Red (V *vs.* Ag/AgCl)	HOMO (eV *vs.* vac)	LUMO (eV *vs.* vac)	Bandgap (eV)
C-face (Batch I)	+0.75	−1.86	−5.15	−2.54	2.61
C-face (Batch II)	+0.73	−2.02	−5.13	−2.41	2.75
C-face (Batch IV)	+0.97	−1.31	−5.37	−3.09	2.28

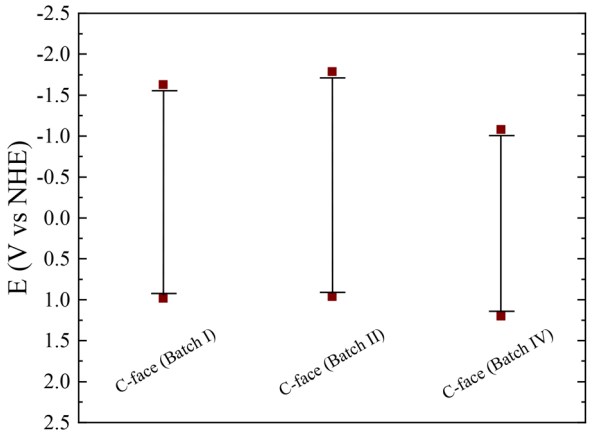

Fig. 6 The conduction band minimum (CBM) and valence band maximum (VBM) potentials of the C-face samples reported on the NHE scales.

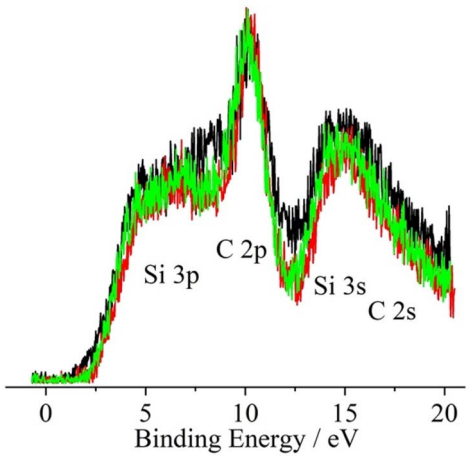

Fig. 7 Al Kα excited XPS valence band for C-face flakes of Batches I, II, and IV. Scan range −1 → 20 eV. The green line refers to the C-face of Batch I, the red line refers to the C-face of Batch II, and the black line refers to the C-face of Batch IV.

SiO_2–84% SiC, and that of the C-face of Batch I is 17% SiO_2–83% SiC.

Accordingly, we can state that more aggressive ECE conditions applied to the C-face flakes of Batch IV resulted in higher surface oxide formation. Regarding the C-face flakes of Batches I and II, the atomic percentages of carbon, silicon, and oxygen are comparable, revealing that the etching conditions in these two Batches are similar. The values of VBM relative to the Fermi level of the 4H-SiC flakes, listed in Table 7, depend on the electrochemical etching condition and the amount of surface oxide. Regarding the data in Table 7, the C-face flakes of Batch IV show a principal and a second VBM value due to the presence of a higher amount of surface oxide. In contrast, the C-face flakes of Batches I and II, with lower oxygen content, exhibit higher VBM values, reflecting the dominant influence of the ECE parameters and the electronic quality. Note that our present study is not really concerned with identifying the nature

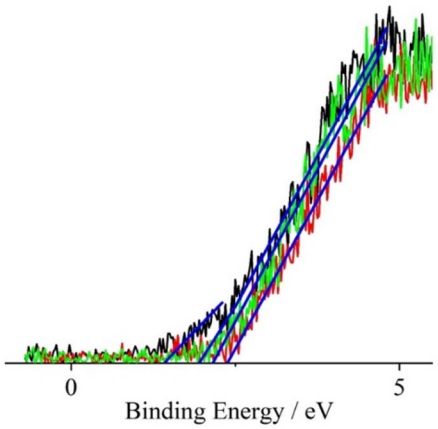

Fig. 8 Al Kα excited XPS valence band edge for the samples in the −1 to 5.5 eV range. The black line refers to the C-face of Batch IV; the green line refers to the C-face of Batch I; the red line refers to Batch II.

of compensating defects, such as cation vacancies, interstitial atoms/ions, more complex defect clusters, or defects at the grain boundaries.[44,45]

Hydrogen production through solar glycerol photoreforming

The solar glycerol photoreforming reaction (eqn (7)) is a sustainable way to obtain green hydrogen.

$$C_3H_8O_3 + 3H_2O \rightarrow 7H_2 + 3CO_2 \quad (7)$$

For an efficient H_2 production, it is necessary to align the bands of the employed semiconductor. In particular, the CB should be more negative of reduction potential of H^+ to H_2 (0 V *vs.* NHE), and VB should be more positive than the oxidation potential of O_2/H_2O (+1.23 V *vs.* NHE) or of the organic compound to a given oxidation product (depending on the specific holes scavenger used, for glycerol +0.004 V *vs.* NHE).[46,47]

It is clear that the oxidation of the organic scavenger was favoured compared to the water oxidation. Therefore, after the solar light absorption, the e^-/h^+ pair was generated (eqn (8)). The presence of organic compounds favours the H_2 evolution. It acts, in fact, as holes scavengers, limiting the electrons/holes recombination. The protons formation was thus favoured from the reaction between the holes and the organic scavenger (eqn (9)). The generated protons are then reduced to H_2 (eqn (10)).

$$SiC + h\nu \rightarrow e^- + h^+ \quad (8)$$

Table 7 VBM values extrapolated *via* XPS measurements of the 4H-SiC C-face flakes (Batches I, II, and IV)

Sample	VBM (eV)
C-face (Batch I)	2.65
C-face (Batch II)	2.71
C-face (Batch IV)	2.28, 1.42

$$C_3H_8O_3 + 3H_2O + 14h^+ \rightarrow 14H^+ + 3CO_2 \quad (9)$$

$$14H^+ + 14e^- \rightarrow 7H_2 \quad (10)$$

The glycerol photoreforming was conducted using electrochemically etched 4H-SiC flakes, both Si- and C-face, under simulated solar irradiation. The obtained H_2 production rates (measured by GC-TCD measurements considering the catalyst amount and the 5 h of simulated solar irradiation) are shown in Fig. 9. The overall H_2 production ranges from a lowest value of 12 μmol g^{-1} h^{-1} up to 275 μmol g^{-1} h^{-1}, depending on Batch and etched SiC face (Si *vs.* C): flakes derived from Batch II perform better than others, while the least productive Batch is IV. Notably, in our previous study, the amount of H_2 generated by (non-porous) 4H-SiC wafers is about 20 μmol g^{-1} h^{-1},[37] thus in good agreement with the minimum amount obtained by using porous flakes. The better performance obtained by some specific Batches (about 10-fold production rates with respect to non-porous wafer) is attributable to a combination of factors derived from morphological and electronic modifications promoted by ECE. In particular, the samples showing the best performance in hydrogen production are the porous flakes from Batches I and II, obtained using an HF concentration of 15 wt% in the electrolyte solution. In particular, decreasing the current density to 42 mA cm^{-2} between Batch I and II, a higher amount of hydrogen was produced. In this case, lowering the current density at the same HF concentration in the electrolyte solution, the oxide formation rate on the surface decreases, and the electrochemical etching process becomes more controlled, compared to Batch I.

In fact, the C-face flakes of Batch II deliver the highest hydrogen production, highlighting the dominant influence of electronic quality.

From the CV measurements, the C-face flakes of Batch II show the most negative conduction band minimum (CBM), consistent with its superior hydrogen evolution performance, followed by the C-face of Batch I. In contrast, varying the HF concentration in Batches III and IV, while keeping the current density constant at 420 mA cm^{-2}, as in Batch I, a decrease in hydrogen production was noted. In Batch III, lowering the HF concentration to 5 wt%, compared to Batch I, limits oxide dissolution, resulting in a less uniform etching process. Finally, in Batch IV, increasing the HF concentration to 30 wt% promotes a more aggressive etching process, increasing surface disorder and defect formation, acting as traps for electrons,[35] showing the lowest photocatalytic activity. Hence, HF concentration plays a crucial role in determining morphology, defect density, and electronic properties, in addition to current density. To note that Batch IV possesses the higher surface SiO_2, which could act as a barrier to charge transfer, thus affecting H_2 production.

A complete glycerol photoreforming should produce a theoretical 2.3 H_2/CO_2 ratio (eqn (7)). Considering the experimental band positions of the C-face samples (Fig. 9) and focusing on the best (Batch II) and the worst one (Batch IV) we measured a H_2/CO_2 ratio of 7.2 for Batch II and 0.2 for Batch IV, highlighting as for this latter sample the more positive VB favors the CO_2 formation, *i.e.* the direct glycerol total oxidation instead of the photoreforming reaction. Moreover, this sample also showed a higher photocatalytic activity in the MB oxidation compared to the C-face of Batch II (Table 3), confirming its preferential promotion of oxidation reactions.

In the case of the C-face of the Batch II sample, the high H_2/CO_2 ratio compared to the theoretical one can be attributed, as reported in the literature, to the formation of intermediates such as 1,3-dihydroxyacetone and glyceraldehyde during the glycerol photoreforming, whose formation led to a further H_2 release.[24,37,48] The formation of these two byproducts was detected with various photocatalysts, such as Pt/TiO_2,[49] Cu_2O/TiO_2,[50] g-C_3N_4 [51] or Ni-based photocatalysts,[52] and although the mechanism could be different with SiC, the high H_2/CO_2 ratio can be reasonably due to the further H_2 release by the same intermediates. Further studies will investigate specifically this aspect.

To conclude, the results demonstrate a strong dependence of hydrogen production on the morphological and electronic properties introduced by the etching conditions.

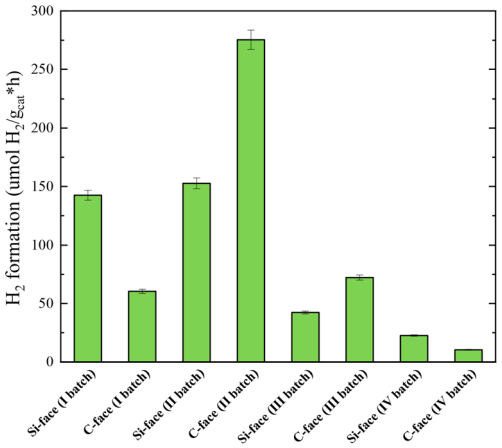

Fig. 9 H_2 production rate by glycerol photoreforming with all the 4H-SiC flakes (Si and C-face).

Conclusions

Overall, the study demonstrates that although porosity significantly influences adsorption behavior and photocatalytic activity for dyes such as Methylene Blue, hydrogen evolution in photocatalytic systems is ultimately constrained by electronic quality. The C-face of 4H-SiC etched under optimal conditions offers the most effective balance, yielding superior hydrogen generation in glycerol photoreforming.

The relationship between porosity and photocatalytic activity is inherently complex. Although high surface area and uniform pore size in the mesoporous range promote dye adsorption and improved reactant diffusion, enhanced adsorption does not necessarily translate into higher dye photocatalytic degradation efficiency. This decoupling between structural and electronic contributions demonstrates that photocatalytic efficiency depends on a delicate balance between geometric accessibility of the material to the molecules and band gap optimization.

While morphology governs adsorption and diffusion, factors such as defect density, band bending, and surface terminations regulate charge separation and interfacial transfer. The C-face, which consistently exhibits bimodal pore-size distributions, typically performs worse than the Si-face; however, Batch IV shows that careful current modulation during etching can suppress recombination sufficiently to achieve comparatively high activity in the dye degradation. On the contrary, the shifting of the band's position due to a peculiar electrochemical etching process was a critical feature to drive the photocatalytic activity towards the oxidation reaction (dyes removal) or the proton reduction to obtain H_2.

From a technological standpoint, porous SiC represents a promising candidate for solar-driven hydrogen production. Its wide band gap provides photochemical stability, while electrochemical etching offers a tunable route to tailor morphology.

Future research should prioritize refining etching strategies, such as implementing pulsed current profiles, adjusting HF concentration, and applying post-etch defect-healing treatments, to better trigger porosity with electronic quality.

Author contributions

V. S.: conceptualization, investigation, methodology, data curation, writing – original draft, formal analysis, writing – review, conceptualization, investigation, methodology, data curation, A. G.: investigation, methodology, data curation, formal analysis, writing – review, and editing. M. C.: investigation, methodology, data curation, formal analysis, writing – review, and editing. L. C.: investigation, methodology, data curation, formal analysis, writing – review, and editing. R. F.: investigation, methodology, data curation, formal analysis, writing – review, and editing. S. S.: investigation, methodology, data curation, formal analysis, writing – review, and editing. A. G.: investigation, methodology, and editing. M. B.: data curation, formal analysis, writing – review, and editing. T. D.: conceptualization, investigation, methodology, writing – review and editing, supervision, project administration, and resources. G. G.: conceptualization, investigation, methodology, writing – review and editing, supervision, project administration, and resources. M. E. F.: conceptualization, investigation, methodology, data curation, writing – original draft, writing – review and editing, supervision, project administration, resources, and funding acquisition.

Conflicts of interest

There are no conflicts to declare.

Data availability

The data supporting this article have been included as part of the supplementary information (SI). This study was carried out using publicly available data for Fig. 4 from *J. Mater. Chem. A*, 2025, **13**, 3034 at https://doi.org/10.1039/d4ta07035f. Supplementary information is available. See DOI: https://doi.org/10.1039/d6ta01058j.

Acknowledgements

The authors gratefully acknowledge the financial support by NextGeneration EU funds, through the MUR-PNRR project SAMOTHRACE – SiciliAn MicronanOTecH Research And Innovation CEnter (project number ECS 00000022). This work was supported by the Evo MAF-Mof PIACERI project (Università di Catania), by the technological platform CERTeM+ (Tours, France) and BRIT (Catania, Italy).

References

1 G. W. Crabtree, M. S. Dresselhaus and M. V. Buchanan, *Phys. Today*, 2004, **57**, 39–44.
2 S. Yadav and P. Malhotra, *Top. Catal.*, 2025, **2025**, 1–25.
3 M. Y. Qi, M. Conte, M. Anpo, Z. R. Tang and Y. J. Xu, *Chem. Rev.*, 2021, **121**, 13051–13085.
4 K. Chen, W. Dong, Y. Huang, F. Wang, J. L. Zhou and W. Li, *J. Environ. Chem. Eng.*, 2025, **13**, 117529.
5 E. I. García-López, L. Palmisano and G. Marcì, *ChemEngineering*, 2023, **7**, 11.
6 I. Merino-Garcia, S. Castro, A. Irabien, I. Hernández, V. Rodríguez, R. Camarillo, J. Rincón and J. Albo, *J. Environ. Chem. Eng.*, 2022, **10**, 107441.
7 A. Fujishima and K. Honda, *Nature*, 1972, **238**(5358), 37–38.
8 X. Chen and S. S. Mao, *Chem. Rev.*, 2007, **107**, 2891–2959.
9 X. Li, J. Lin, D. Zhang, Z. Xiong, X. He, M. Yuan and M. Wang, *Resour. Policy*, 2020, **67**, 101685.
10 J. Antonio Abarca, G. Díaz-Sainz, I. Merino-Garcia, A. Irabien and J. Albo, *J. Energy Chem.*, 2023, **85**, 455–480.
11 J. A. Abarca, I. Merino-Garcia, G. Díaz-Sainz, M. Perfecto-Irigaray, G. Beobide, A. Irabien and J. Albo, *Catal. Today*, 2024, **429**, 114505.
12 W. Tu, Y. Zhou and Z. Zou, *Adv. Funct. Mater.*, 2013, **23**, 4996–5008.
13 X. Dai, M. Xie, S. Meng, X. Fu and S. Chen, *Appl. Catal., B*, 2014, **158–159**, 382–390.
14 H. Huang, Y. Jin, Z. Chai, X. Gu, Y. Liang, Q. Li, H. Liu, H. Jiang and D. Xu, *Appl. Catal., B*, 2019, **257**, 117869.
15 M. Z. Rahman, F. Raziq, H. Zhang and J. Gascon, *Angew. Chem., Int. Ed.*, 2023, **62**, e202305385.
16 D. Zhuang and J. H. Edgar, *Mater. Sci. Eng. R: Rep.*, 2005, **48**, 1–46.
17 J. H. Tan, Z. zhan Chen, W. Y. Lu, Y. Cheng, H. He, Y. H. Liu, Y. J. Sun and G. J. Zhao, *Nanoscale Res. Lett.*, 2014, **9**(1), 1–5.
18 M. Cabello, V. Soler, G. Rius, J. Montserrat, J. Rebollo and P. Godignon, *Mater. Sci. Semicond. Process.*, 2018, **78**, 22–31.
19 W. Wang, X. Lu, X. Wu, Y. Zhang, R. Wang, D. Yang and X. Pi, *Adv. Mater. Interfaces*, 2023, **10**, 2202369.
20 M. Barcellona, V. Spanò, R. Fiorenza, S. Scirè, T. Defforge, G. Gautier and M. E. Fragalà, *J. Mater. Chem. A*, 2025, **13**, 3034–3044.
21 G. Gautier, F. Cayrel, M. Capelle, J. Billoué, X. Song and J. F. Michaud, *Nanoscale Res. Lett.*, 2012, **7**, 2–22.
22 R. Sánchez-Salcedo, P. Sharma and N. H. Voelcker, *ACS Appl. Mater. Interfaces*, 2025, **17**, 2814–2843.

23 Z. Liu, W. Ye, J. Zheng, Q. Wang, G. Ma, H. Liu and X. Wang, *Regener. Biomater.*, 2020, **7**, 453–459.
24 S. A. Balsamo, R. Fiorenza, M. T. A. Iapichino, F. J. Lopez-Tenllado, F. J. Urbano and S. Sciré, *Mol. Catal.*, 2023, **547**, 113346.
25 E. La Greca, M. T. Armeli Iapichino, M. C. Herrera Beurnio, F. J. Urbano Navarro, L. F. Liotta, S. Scirè and R. Fiorenza, *Catalysts*, 2025, **15**, 555.
26 G. Gautier, J. Biscarrat, D. Valente, T. Defforge, A. Gary and F. Cayrel, *J. Electrochem. Soc.*, 2013, **160**, D372–D379.
27 Y. Shishkin, W. J. Choyke and R. P. Devaty, *J. Appl. Phys.*, 2004, **96**, 2311–2322.
28 S. Rysy, H. Sadowski and R. Helbig, *J. Solid State Electrochem.*, 1999, **3**, 437–445.
29 J. Matthew, *Surf. Interface Anal.*, 2004, **36**, 1647.
30 A. Gulino, *Anal. Bioanal. Chem.*, 2013, **405**, 1479–1495.
31 G. Greczynski and L. Hultman, *Angew. Chem.*, 2020, **132**, 5034–5038.
32 A. Ferlazzo, A. Gulino and G. Neri, *Environ. Sci.:Adv.*, 2024, **3**, 1392–1399.
33 M. T. A. Iapichino, R. Fiorenza, V. Patamia, G. Floresta, A. Gulino, M. Condorelli, G. Impellizzeri, G. Compagnini and S. Sciré, *Catal. Commun.*, 2024, **187**, 106850.
34 S. Alkaykh, A. Mbarek and E. E. Ali-Shattle, *Heliyon*, 2020, **6**, e03663.
35 X. Han, A. Qian, L. Ye, M. Fan, J. Yu, C. Zhang, Y. Zheng and Q. Yang, *Mol. Chem. Eng.*, 2025, **1**, 100001.
36 P. R. Jubu, O. S. Obaseki, D. I. Ajayi, E. Danladi, K. M. Chahrour, A. Muhammad, S. Landi, T. Igbawua, H. F. Chahul and F. K. Yam, *J. Opt.*, 2024, **53**, 5054–5064.
37 F. Florio, R. Fiorenza, A. Ferlazzo, M. E. Fragalà, M. Barcellona and A. Gulino, *Mater. Today Sustain.*, 2025, **31**, 101171.
38 Z. Ji, Z. Gao, T. Zhang and A. Kitai, *Appl. Surf. Sci.*, 2025, **694**, 162797.
39 J. Klein, L. Kampermann, B. Mockenhaupt, M. Behrens, J. Strunk and G. Bacher, *Adv. Funct. Mater.*, 2023, **33**, 2304523.
40 A. Ferlazzo, M. Chelly, A. Gulino and G. Neri, *J. Agric. Food Chem.*, 2025, **73**, 25628–25635.
41 C. M. Cardona, W. Li, A. E. Kaifer, D. Stockdale, G. C. Bazan, C. M. Cardona, W. Li, A. E. Kaifer, D. Stockdale and G. C. Bazan, *Adv. Mater.*, 2011, **23**, 2367–2371.
42 V. V. Pavlishchuk and A. W. Addison, *Inorg. Chim. Acta*, 2000, **298**, 97–102.
43 R. Mahapatra, A. K. Chakraborty, A. B. Horsfall, N. G. Wright, G. Beamson and K. S. Coleman, *Appl. Phys. Lett.*, 2008, **92**, 042904.
44 S. Millesi, M. R. Catalano, G. Impellizzeri, I. Crupi, G. Malandrino, F. Priolo and A. Gulino, *Mater. Sci. Semicond. Process.*, 2017, **69**, 32–35.
45 A. Gulino, A. E. Taverner, S. Warren, P. Harris and R. G. Egdell, *Surf. Sci.*, 1994, **315**, 351–361.
46 Z. H. N. Al-Azri, W. T. Chen, A. Chan, V. Jovic, T. Ina, H. Idriss and G. I. N. Waterhouse, *J. Catal.*, 2015, **329**, 355–367.
47 C. M. Rueda-Navarro, B. Ferrer, H. G. Baldoví and S. Navalón, *Nanomaterials*, 2022, **12**, 3808.
48 F. J. López-Tenllado, R. Estévez, J. Hidalgo-Carrillo, S. López-Fernández, F. J. Urbano and A. Marinas, *Catal. Today*, 2022, **390–391**, 92–98.
49 M. M. R. Oliveira, E. J. R. Sousa, L. S. Bomfim, M. M. Duarte, A. J. M. Sales, R. A. Antunes, S. F. Santos, F. M. T. Luna, R. S. Araújo, P. K. J. Robertson and B. C. B. Salgado, *ACS Omega*, 2026, **11**, 9312–9324.
50 V. Maslova, A. Fasolini, M. Offidani, S. Albonetti and F. Basile, *J. Ind. Eng. Chem.*, 2023, **118**, 247–258.
51 A. Ajanovic, M. Sayer and R. Haas, *Catal. Today*, 2024, **430**, 114548.
52 M. Eisapour, T. Roostaei, M. Kaur, J. Hu, H. Zhao and Z. Chen, *Ind. Eng. Chem. Res.*, 2025, **64**, 20516–20524.

